Effect of double diffusion processes in the deep ocean on the distribution and dynamics of particulate and dissolved matter: a case study in Tyrrhenian Sea

Xavier DURRIEU DE MADRON[1]*, Paul BLIN[1], Mireille PUJO-PAY[2], Vincent TAILLANDIER[3], Pascal CONAN[2,4]

[(1)] CEFREM, CNRS-Université de Perpignan Via Domitia, Perpignan, France

[(2)] LOMIC, CNRS-Sorbonne Université, Banyuls/Mer, France

[(3)] LOV, CNRS-Sorbonne Université, Villefranche/Mer, France

[(4)] OSU STAMAR, CNRS-Sorbonne Université, Paris, France

Correspondence to: Xavir Durrieu de Madron (demadron@univ-perp.fr)

Abstract: This study examines CTD, ADCP and optical data collected during the PERLE-3 cruise in March 2020 between the surface and 2000 m depth over an east-west section of the Tyrrhenian Sea in the Mediterranean. The focus is on the impact of double diffusion processes, in particular salt fingering, on the distribution and dynamics of particulate and dissolved matter. The staircases develop at the interface between the warm, saline Eastern Intermediate Water (EIW) and the colder, less saline Tyrrhenian Deep Water (TDW) in the centre of the basin with low hydrodynamic energy. The results show that thermohaline staircases formed by salt fingering significantly influence particle sedimentation and biogeochemical cycling in deep ocean environments by altering vertical flux patterns. These density steps create distinct vertical layers that act as physical barriers, slowing the descent of particles and facilitating their retention and aggregation. The staircases also affect dissolved matter by creating pronounced concentration gradients of oxygen and nutrients, which can influence microbial activity and nutrient fluxes.

Keywords: Mediterranean, Tyrrhenian Sea, Double diffusion, Salt fingering, Suspended particulate matter, Particle size spectra, Nitrate, Mineralization

a supprimé: will be

a supprimé: salty

a supprimé: Levantine

a supprimé: L

a supprimé: salty

a supprimé: Retention of fine particles at density gradients promotes the formation of larger aggregates, affecting particle size distribution.

a supprimé: cycling

Graphical abstract:

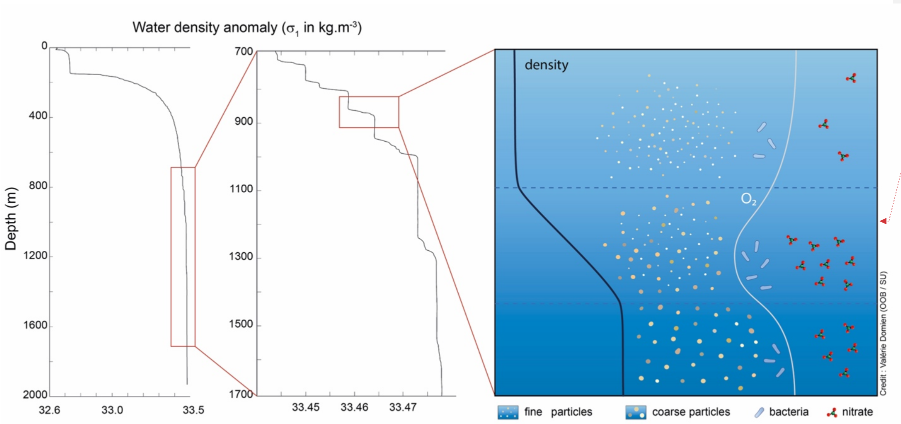

1. Introduction

Gravitational settling of biologically derived particles, produced by marine plankton in the surface layer, is the primary driver of vertical fluxes of material in the deep ocean (Newton and Liss, 1990). In general, vertical mass fluxes of particles in the ocean decrease exponentially with depth due to particle degradation and the increasing density of seawater (Omand et al., 2020). Marine particles have a wide range of sizes, from micrometres (clays) to centimetres (organic detritus). Particles generally tend to agglomerate to form aggregates of different sizes, shapes, densities, and characteristics (Kiko et al., 2022). The change in geometry of the aggregates as well as their excess density compared to seawater are the factors that determine their sedimentation rate.

The water column in the ocean is composed by the superposition of water masses with generally distinct thermohaline characteristics and often distant origins. Large density interfaces, associated with strong vertical gradients in temperature (~0.25 °C m^{-1}) at seasonal thermoclines, or salinity (~0.5 g kg^{-1} m^{-1}) at river plumes can occur in the upper ocean, resulting in the retention of the less dense particles. In the deep ocean temperature and salinity gradients are much weaker, and the effect of particle size becomes greater than the effect of density excess, so that settling velocity generally increases with particle size. Thus settling velocities in the open ocean are on the order of 5 x10^{-4} mm s^{-1} to 1 mm s^{-1} for particles ranging from 2 µm to 300 µm (McCave, 1975).

However, in the deep ocean, in the transition zones between two water masses, areas of enhanced density gradients can occur due to double diffusion processes, in particular those associated with salt fingers. Salt fingering is a common process in the ocean (Kunze, 2003; Radko, 2013; Radko et al., 2014). It requires a stably stratified water column, where a layer of

a mis en forme : Retrait : Gauche : 0 cm, Première ligne : 0 cm
a supprimé: /
a mis en forme : Exposant
a supprimé: /
a supprimé: /
a mis en forme : Exposant
a mis en forme : Exposant
a supprimé: is
a supprimé: /
a supprimé: /
a mis en forme : Exposant
a mis en forme : Exposant

warm, saline water overlies a layer of cooler, less saline water. Because molecular diffusion of temperature is about 100 times faster than that of salinity, the salinity interface initially remains essentially unchanged as temperature exchange occurs across it. As a result, the saltier water above this thin mixed layer of average temperature becomes denser than the less saline water below. This leads to salt finger instabilities at the interface: the saltier water sinks and the less saline water rises. The mixing process is then repeated at the new interfaces, resulting in a progressive thickening of the mixed layer and an increase in the vertical density gradients on either side of the interface. If favourable conditions persist, step structures can develop and reach thicknesses of several tens of meters (Radko et al., 2014). These staircases exhibit temperature and salinity steps ranging between 0.001 and 0.019°C and 0.001 and 0.2 g kg^{-1}, respectively (Van Der Boog et al., 2021).

Various experimental and numerical studies have explored the impact of density interfaces on the sedimentation of particulate material, but to our knowledge very little research has been applied to the deep oceanic environment. Laboratory experiments conducted for a variety of individual particles geometries and densities (e.g. Prairie et al., 2013; Mrokowska, 2018; Doostmohammadi and Ardekani, 2014; Doostmohammadi and Ardekani, 2015; Verso et al., 2019) generally show a decrease in settling velocity, as well as a reorientation of the particles, during their passage through the transition layer formed by the density interface. The initial decrease is followed by an increase, once the particle reaches the base of the interface, but this settling velocity is always smaller in the lower layer due to its higher density. The initial decrease in velocity in the interface is likely due to the entrainment of less dense water by the particles and the drag of their wake as they cross the interface. Finally, Maggi (2013) shows that sedimentation rates are very well correlated with size for mineral particles, but are much less clear for biomineral or biological material. Thus, the sedimentation rate of a solid particle alone will depend almost exclusively on its size. This is not the case for aggregates, where composition, shape, excess density and porosity must also be taken into account. Kindler et al. (2010) demonstrated that slowly sinking particles, like highly porous aggregates, can be retained and therefore accumulate at density interfaces, increasing the likelihood of collisions and subsequent aggregation. They suggested that this increase in retention time may affect carbon transformation through increased microbial colonization and utilization of particles and release of dissolved organics.

The Mediterranean Sea is a prime location for the observation and study of thermohaline staircases due to its unique hydrographic conditions. The study presented here focuses on the behaviour of particulate matter and dissolved elements in the Tyrrhenian Sea (Fig. 1a), a region known to be favourable for salt fingers with the formation of large staircases at the transition between intermediate and deep waters (Durante et al., 2019). The Tyrrhenian Sea has a complex circulation pattern characterised by three main water masses: Atlantic Water (AW) at the surface, Eastern Intermediate Water (EIW) at intermediate depths and Tyrrhenian Deep Water (TDW) in the deeper layers (Millot and Taupier-Letage, 2005; Iacono et al., 2021). Note that the names of the water masses follow the nomenclature recommended by Schroeder et al. (2024). The surface circulation shows strong seasonal variability, with a basin-wide cyclonic pattern in winter, which weakens and becomes more complex in summer. The EIW, formed in the eastern Mediterranean Basin, enters through the Strait of Sicily. It is found throughout the Tyrrhenian Sea at depths between 200 and 700 m. It participates in the cyclonic flow and exits through the Corsican and Sardinian channels. The deep circulation, involving the TDWs, is defined as resulting from the mixing of the deep waters of the western Mediterranean with the

a supprimé: salty

a supprimé: salty

a supprimé: salty

a supprimé: Such thermohaline diffusive convection

a supprimé: salty

a supprimé: typical

a supprimé: gradients

a supprimé: on the order of

a supprimé: /m

a supprimé: /

a supprimé: /m

a mis en forme : Exposant

a supprimé: There is also the case of a layer of turbid water overlying clearer, denser water, such as for hypopycnal particle-laden river plumes (e.g. Green, 1987; Hoyal et al., 1999; Hoshiba et al., 2021). Instabilities may arise as a result of the different diffusivities of each of the constituents (sediment, temperature, salinity) (Parsons and Garcia, 2000). Both double diffusive and settling driven convection processes can drive fingering and mixing at the interface, and therefore, double diffusive sedimentation can add up to the gravitational settling velocity and enhance the scavenging of particles from the buoyant turbid plume. However, for large particles and dilute concentrations, the flux is more dominated by gravitational settling and the double diffusive sedimentation of suspended particles is considered negligible (e.g. Davarpanah Jazi and Wells, 2016).¶

a supprimé: its

intermediate and deep waters of the eastern basin (Sparnocchia et al., 1999) but also from the possibility of local formation (Fuda et al., 2002). Staircase structures, characterized by remarkable spatial and temporal stability, extend over most of the central basin at depths between 600 and 2500 m, with individual layers spanning tens or even hundreds of meters in thickness. These persistent formations have been consistently observed and documented over several decades, demonstrating their long-term coherence in the region (Johannessen and Lee, 1974; Molcard and Tait, 1977; Zodiatis and Gasparini, 1996; Sparnocchia et al., 1999; Falco et al., 2016).

a mis en forme : Anglais (E.U.)

a supprimé: The warm and saline Levantine Intermediate Water (LIW), formed in the eastern Mediterranean Basin, is found throughout the Tyrrhenian Sea at depths between 200 and 700 m. Deeper is the Tyrrhenian Deep Water (TDW), colder and less saline, formed by the mixing of the deep waters of the western Mediterranean with the intermediate and deep waters of the eastern basinFalco et al., 2016). Staircase structures, which extend over most of the central basin, are found at depths between 600 and 2,500 m and are tens or even hundreds of meters thick

a mis en forme : Anglais (E.U.)

a mis en forme : Anglais (E.U.)

a supprimé: intermediate

The dataset used in this work was obtained from the PERLE-3 cruise (Pujo-Pay et al., 2020) whose main objective is to study the formation of Levantine intermediate waters in the eastern basin and their fate and transformation along their course in the Mediterranean Sea. Here, we focused on a section between the Bay of Naples and southern Sardinia, which cuts across the Tyrrhenian Sea from east to west. The data collected included hydrological parameters (temperature, salinity, density), hydrodynamic parameters (current velocity and direction), and particulate (turbidity, large particle abundance) and dissolved (oxygen, nitrate) parameters in the upper 2000 m of the water column. The two questions addressed here are (1) what are the characteristics and development conditions of the notable staircase structures observed during this cruise, and (2) what is the impact of these staircases on the distribution of dissolved and particulate matter. The answers to these two questions will provide new insights into the ecological consequences of these small-scale structures.

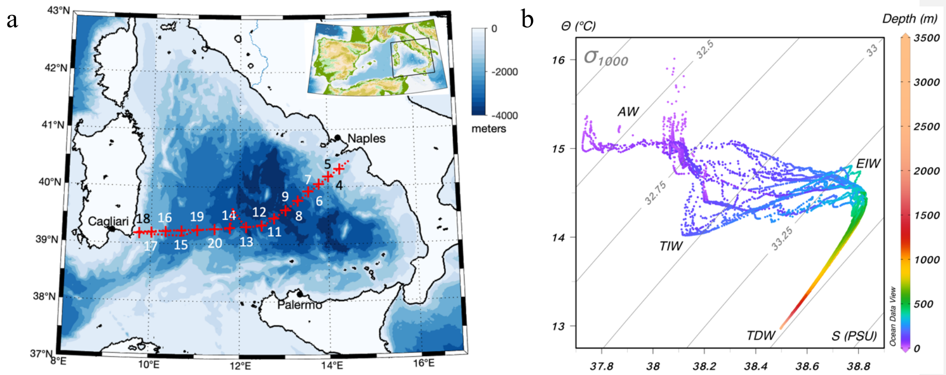

Figure 1 (a) Map of the stations carried out during part of the PERLE-3 cruise (14–16 March 2020) in the Tyrrhenian Sea. The route followed by the ship is indicated by the dotted red line. The northward deviation in the centre of the basin is associated with the recovery of the profiling float. (b) *Θ-S diagram for the different stations of the transect and associated water masses (AW, Atlantic Water; TIW, Tyrrhenian Intermediate Water; EIW, Eastern Intermediate Water; TDW, Tyrrhenian Deep Water), with depth in color.*

a supprimé: *Stations 9 and 20, indicated by stars, are the two stations chosen to characterize the water column respectively with and without staircases between intermediate and deep water*

a mis en forme : Anglais (E.U.)

a supprimé: *M*

a supprimé: *Modified*

a supprimé: *LIW*

a supprimé: *Levantine*

2. Material and Methods

2.1 Hydrographical and optical data

This hydrographic survey of the Tyrrhenian Sea was conducted in March 2020 as part of the PERLE-3 cruise, which was unexpectedly shortened due to the outbreak of the COVID-19 pandemic. It includes 16 stations for which hydrological profiles were obtained between the surface and 2000 m with a Seabird 911+ CTD-O2 probe mounted on a rosette carrying 22 twelve-liter Niskin bottles. Additional optical sensors (Wetlabs C-Star 0.25 m pathlength transmissometer at 650 nm wavelength, Seabird Suna V2 UV nitrate sensor, Hydroptic Underwater Vision Profiler UVP-5) were connected to the probe.

Data from the CTD sensors and the transmissometer were recorded at a frequency of 24 Hz. Data were therefore acquired every 2 cm vertically at a descent rate of 1 m s^{-1}. The temperature and conductivity sensors provided measurements with a resolution of 2.10^{-4} °C (4.10^{-5} S/m) and an accuracy of 2.10^{-3} °C (3.10^{-4} S m^{-1}), respectively. The dissolved oxygen sensor provided measurements with a resolution of 0.2 µmol kg^{-1}. The transmissometer has a resolution of 1.25 mV over a range of 0 to 5 V (WET Labs, Inc., 2011), giving a beam attenuation coefficient [BAC= -4×ln (T%), where T% is the transmittance in %] and resolution of 10^{-3} 1/m. The UVP-5 (Picheral et al., 2010) is a stand-alone camera mounted on the CTD/rosette frame to quantify the vertical distribution of large particles and zooplankton. Images were acquired at a frequency of up to 6 Hz, i.e. on average every 20 cm at a descent rate of 1 m/s. The small size limit of the UVP-5 is determined by the optical resolution (94.7 µm corresponding to 1 pixel), while the large size limit is determined by the volume of water illuminated (1.02 l).

The stand-alone Seabird Suna V2 UV nitrate sensor attached to the CTD collected data at 1 Hz from the surface down to 2000 m. It uses ultraviolet absorption spectroscopy to measure nitrate in situ. A good correlation was observed with bottle measurements over the entire water column collected during the cruise at station PERLE3-10 (R^2= 0.99, N=27 samples, p <10^{-5}, $NO_{3\ SUNA} = 0.991 \times NO_{3\ btl} - 0.116$).

The CTD data processing was performed with the SBE Data Processing software, and derived variables (potential temperature, salinity, potential density anomaly, and density ratio) were estimated based on the TEOS-10 toolbox (IOC, SCOR and IAPSO, 2010).

The transmissometer provides a beam attenuation coefficient (BAC), which is linearly correlated with particle concentration. This signal is influenced by the size and composition of the particles (Hill et al., 2011). Due to their preponderance and larger surface to volume ratio, this signal is essentially sensitive to the finest (sub-micron to micron) particles. As a result, turbidity spikes causes by the rare passage of large particles through the beam were eliminated by smoothing (Giering et al., 2020).

The UVP provides quantitative data of the abundance (in number of particles per litre, # L^{-1}) of large particles for the different size classes between 80 µm and 2000 µm (equivalent circular diameter) was estimated from the raw images (Picheral et al., 2010). It is refer in the text as large particulate matter (LPM). The UVP data were then processed to estimate the particle size distribution, which was modelled using a typical power law of the form $N(d) = C \times d^{-\alpha}$, where C represents a constant, d stands for particle diameter, and –α denotes the Junge index (Guidi et al., 2009). The Junge index is determined through linear regression involving

a supprimé: Shipborne
a supprimé: Hydrographical
a mis en forme : Retrait : Première ligne : 1,25 cm
a supprimé: (
a supprimé: 0.0002
a mis en forme : Exposant
a supprimé: 0.002
a supprimé: 0,000 3
a supprimé: /
a mis en forme : Exposant
a mis en forme : Exposant
a mis en forme : Exposant
a mis en forme : Exposant
a supprimé: /
a mis en forme : Exposant
a supprimé: instrument
a supprimé: are
a supprimé: conservative
a supprimé: absolute
a supprimé: Brunt-Väisälä frequency
a supprimé: Turner angle
a supprimé: The transmissometer signal was associated with the finest and most numerous particles (~ 1–10 µm), while larger particles (from 80 µm) were seen by the UVP. For transmissometer data, …
a supprimé: the
a supprimé: due
a supprimé: to
a mis en forme : Non Surlignage
a mis en forme : Non Surlignage
a mis en forme : Non Surlignage
a supprimé: For UVP data,
a mis en forme : Anglais (E.U.)
a supprimé: l
a supprimé:
a mis en forme : Non Exposant/ Indice

log-transformed values of N(d) and d. The calculation was performed on the size range between 80 and 400 µm, in order to consider only the most abundant particles, which represent up to 99% of the total number observed and whose concentration is greater than 1 particle per litre (Table A1). The Junge index, α, varies between 2.5 and 4.5 for this data set. A slope of the differential particle size distribution of 4 indicates an equal amount of mass in logarithmically increasing size intervals. Higher values indicate a greater dominance of fine particles within the particle population, while lower values are associated with particle populations enriched in larger particles.

a supprimé: microns

a supprimé: 4

Another CTD data set was collected from a BGC-Argo profiling float (WMO 6902903). This float was equipped with SBE-41CP pumped CTD with a sampling rate of 0.5 Hz and an instrumental precision of 0.01 for salinity, 0.002 °C for temperature and 2.4 dbar for pressure. CTD profiles were collected during an ascent from the parking depth to the surface, which took between 3 and 6 hours, depending on the depth, at a nominal vertical speed of 0.1 m s^{-1}. The profiling float collected data for almost 2 years, between 23 June 2018 and 15 March 2020 (date of recovery during the PERLE-3 cruise). It remained in the centre of the Tyrrhenian Basin (between 39.1-39.7° N, 11.6-12.8° E) during this period. The resulting time series of CTD profiles includes 16 profiles between 0 and 1000 m from June 23 to July 6, 2018, and 118 profiles between 0 and 2000 m from July 13, 2018 to March 15, 2020, with a time resolution of 7 days until October 2019, then 3 days thereafter.

The filtering step proved to be very important, given the scales on which the study focused, to remove the spikes and reduce the noise of the signal while maintaining the best vertical resolution. The 24 Hz raw data were subjected to outlier removal using two successive moving median filters with window lengths of 7 and 5 scans, respectively. The data were then binned at 1 m intervals and smoothed with a Loess regression filter. For temperature, salinity, and potential density anomaly signals, the loess regression smoothing window length was 10 scans (10 metres). For dissolved oxygen, nitrate, beam attenuation coefficient, UVP, and Junge index signals we applied a Loess regression smoothing with a window length of 50 scans (50 metres).

Thermohaline staircases are characterized by alternating mixed layers, which are thick regions of nearly constant temperature, salinity and density, and interfaces, which are thin layers with sharp changes in temperature salinity, and density. Step structures were defined based on temperature and salinity profiles between 500 and 2000 m depth, following the procedure described in Durante et al. (2019). Relative maxima in the vertical gradient of salinity and potential temperature are used to identify interfaces that form well-marked steps and delimit a well-mixed layer. Gradient thresholds of 10^{-4}°C m^{-1} for potential temperature and 5 x10^{-4} PSU m^{-1} for salinity were used.

2.2 Acoustical data

a supprimé: Shipborne

a supprimé: a

a supprimé: for current and backscatter index

a supprimé: -borne

During the PERLE-3 survey, two shipboard Acoustic Doppler Current Profilers – S-ADCPs – collected continuous current data from 21 m to 1200 m depth. The first S-ADCP was an RDI OS150 with an acoustic frequency of 150 kHz, a sampling rate of 1 Hz, and a cell size of 8 m, allowing a total range of 220 m. The second S-ADCP was an RDI OS38 with an acoustic frequency of 38 kHz, a sampling rate of 1 Hz, and a cell size of 8 m, allowing a maximum range of 1200 m. Data averaged over a 2-min period were concatenated and processed using Cascade V7.2 processing software (Kermabon et al., 2018) to compute horizontal ocean current velocities with a spatial resolution of 2 km, corrected for navigation and ship attitude parameters, and filtered according to various quality criteria (i.e., thresholds on vertical velocity error, vertical shear, correlation, minimum percentage of valid ensembles, Kermabon et al., 2018). Bathymetry (Etopo 1 with 1 arc-minute resolution) was incorporated in the processing to account for bottom detection. The profile data for the meridional and zonal components of the current for the two S-ADCPs were combined to obtain a complete profile between 21 and 1200 m depth with maximum resolution in the surface layer.

In addition to the S-ADCP current measurements, current data between the surface and 2000 m depth were also collected using a dual-head Lowered-Acoustic Doppler Current Profiler (L-ADCP) system. These measurements were collected with two RDI Workhorse 300 kHz current meters mounted on the CTD frame, one looking up and one looking down. The vertical profiling resolution was 8 m. The data were processed by the velocity inversion method using version IX of the LDEO software (Thurnherr, 2021). Qualified external data (CTD, S-ADCP, GPS) are used to process the L-ADCP data. The horizontal current profiles generated by the L-ADCPs were combined with the current profiles obtained by the S-ADCPs to obtain current sections between the 21 and 2000 m. Vertical ocean velocities were calculated using the LADCP_w_ocean utility from combined raw L-ADCP and CTD data (Thurnherr, 2022). The upward and downward looking data were processed separately and combined during post-processing to provide vertical velocity profiles for the downcast and upcast.

The data from the 38 KHz S-ADCP were also used to derive the acoustic backscatter index (BI, Mullison, 2017), which is a proxy for the abundance of centimetre-scale reflectors (organic detritus, zooplankton, micronecton…) in the water column. This derivation takes into account the absorption and geometric dispersion of sound $BI = K_C*(RL-Er) + (TL_w + TL_g)$, where K_C is the conversion factor (*count to decibels*) of the ADCP used, RL the received signal, Er the signal noise, TL_w and TL_g are the absorption and geometric transmission losses of the acoustic signal in water respectively.

2.3 Selection of representative stations

The vertical profiles of key thermohaline (temperature, potential, salinity, potential density anomaly), particulate (beam attenuation coefficient, large particulate matter abundance, Junge index) and biogeochemical (dissolved oxygen, nitrate, apparent oxygen utilization) parameters are presented here for two contrasted stations, one with well-developed thermohaline staircases (station 9), the other without significant staircase (station 20). Station 9 was chosen as a representative station for the processes occurring at the density interfaces, while station 20 was chosen as a reference station. Later, in the discussion of the effect of staircases on particle settling and degradation, several examples will be presented for several stations (8, 9 and 11).

a supprimé: is
a supprimé: was added
a supprimé: L-ADCP (
a supprimé:)
a supprimé: looker
a supprimé: [
a supprimé:]
a supprimé: [
a supprimé:]
a supprimé: [
a supprimé:]
a supprimé: [
a supprimé:]
a supprimé: dispersion factors

3. Results

3.1 Hydrological and hydrodynamical features along the section

3.1.1 Temperature, salinity, oxygen, and nitrate

The temperature-salinity diagram (Fig. 1b) and the basin cross-section (Fig. 2) clearly identify the distribution of the water masses present in the study area. As in Falco et al. (2016), we used the isohaline 38.72 as the minimum salinity value to identify the shallowest and deepest levels of the EIW. The Atlantic Water (AW), which extends in the upper 200 m of the water column, has a higher temperature and lower salinity to the east. To the west, the colder Tyrrhenian Intermediate Water (TIW) can be distinguished at about 150 m depth. The warmer, saltier, and oxygen-depleted core of the Eastern Intermediate Water (EIW) is found at depths between 300 and 600 m, as illustrated in Fig. 2 (sections a, b, and c). The core of the colder and less saline Tyrrhenian Deep Water (TDW) is visible beyond 1200 m depth (Fig. 2a and b).

In March, the nitrate distribution in the Tyrrhenian Sea (Fig. 2d) shows a nutrient-poor surface layer and a nutrient-rich deep layer, typical of oligotrophic conditions. Near the surface, nitrate concentrations are low, about 1 µmol kg^{-1}, due to biological uptake. With increasing depth, nitrate concentrations increase. At intermediate depths (250–650 m) they range from 4 to 7 µmol kg^{-1}, indicating a transition zone with maximum vertical gradients. In deeper waters, concentrations reach 7 to 9 µmol kg^{-1} due to decomposing organic matter. The anticyclonic eddy around 12°E and the boundary current, especially over the eastern part of the section, modify the intermediate water depth (EIW) by a few hundred metres without significantly affecting the deep water depth (TDW). This deepening affects the distribution of oxygen and nitrate, which increase less rapidly with depth under these structures.

a

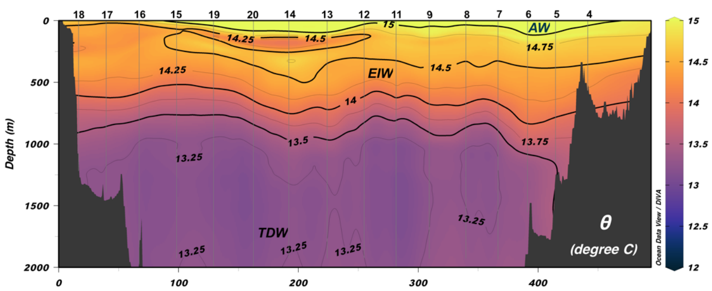

a supprimé: 2.3 Profiling float CTD data
Another CTD data set was collected from a BGC profiling float (WMO 6,902,903). This float is equipped with SBE-41CP pumped CTDs with a sampling rate of 0.5 Hz and an instrumental precision of 0.01 for salinity, 0.002 °C for temperature and 2.4 dbar for pressure. CTD profiles are collected during an ascent from the parking depth to the surface, which takes approximately 3 hours at a nominal vertical speed of 0.1 m/s.
The BGC-Argo float collected data for almost 2 years, between 23 June 2018 and 15 March 2020 (date of recovery during the PERLE 3 cruise). It remained in the centre of the Tyrrhenian Basin (between 39.1-39.7° N, 11.6-12.8° E) during this period. The resulting time series of CTD profiles includes 16 profiles between 0 and 1000 m from June 23 to July 6, 2018, and 118 profiles between 0 and 2000 m from July 13, 2018 to March 15, 2020, with a time resolution of 7 days until October 2019, then 3 days thereafter.

a supprimé: 2.4 Staircases detection
Step structures were defined based on temperature and salinity profiles between 500 and 2000 m depth, following the procedure described in Durante et al. (2019). Relative maxima in the vertical gradient of salinity and potential temperature are used to identify interfaces that form well-marked steps and delimit a well-mixed layer. Gradient thresholds of 10-4°C/m for potential temperature and 5 x10-4 PSU/m for salinity were used.

a supprimé: L
a supprimé: M
a supprimé: LIW
a supprimé: salty
a supprimé: /
a mis en forme : Exposant
a supprimé: /
a mis en forme : Exposant
a supprimé: /
a mis en forme : Exposant
a mis en forme : Non Surlignage
a supprimé:
a mis en forme : Retrait : Première ligne : 0 cm

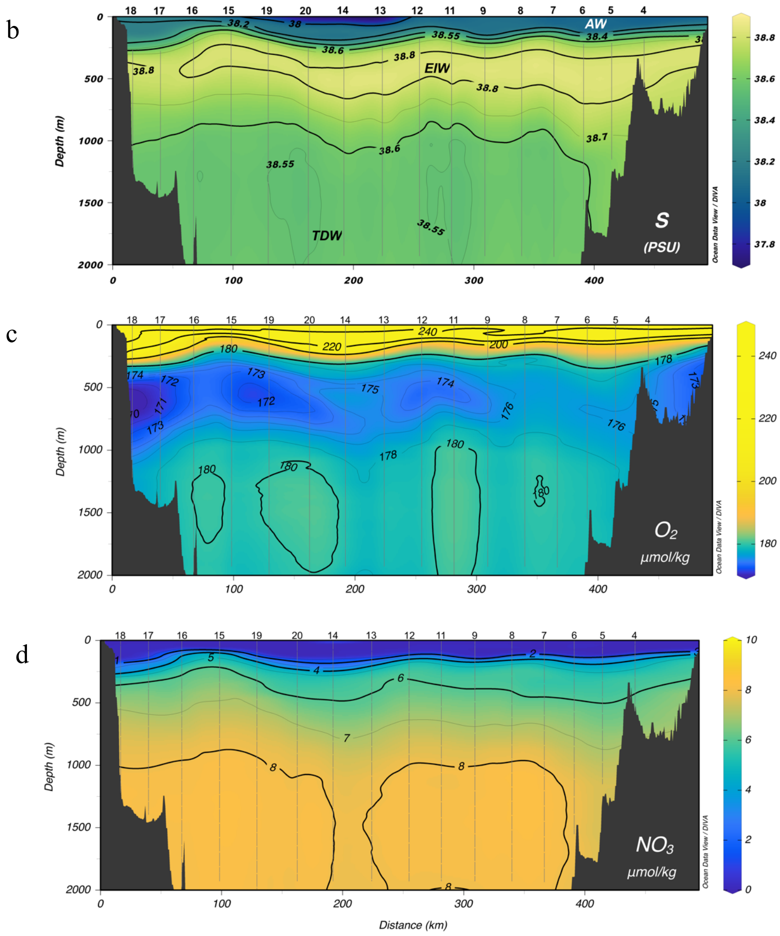

Figure 2: Cross-basin section of (a) potential temperature, (b) salinity, (c) dissolved oxygen, and (d) nitrate for the PERLE-3 cruise (March 2020).

3.1.2 Currents

The dynamic topography and currents measured in the water column during PERLE-3 reveal the presence of two large mesoscale eddies in the centre of the basin with speed of typically 10-15 cm s^{-1} (Fig. 3a, b). The cyclonic eddy at 10.5° E extends to a depth of about 200 m, while the eddy at 12° E extends to more than 500 m. The deep current running along the eastern edge of the basin defines the general along-slope cyclonic circulation. Below the

a supprimé: maximum velocities
a supprimé: about ~30
a supprimé: /
a mis en forme : Exposant

EIW core, i.e. at 600 m depth, the currents are very weak, of the order of a few cm s^{-1} (Fig. 3 c).

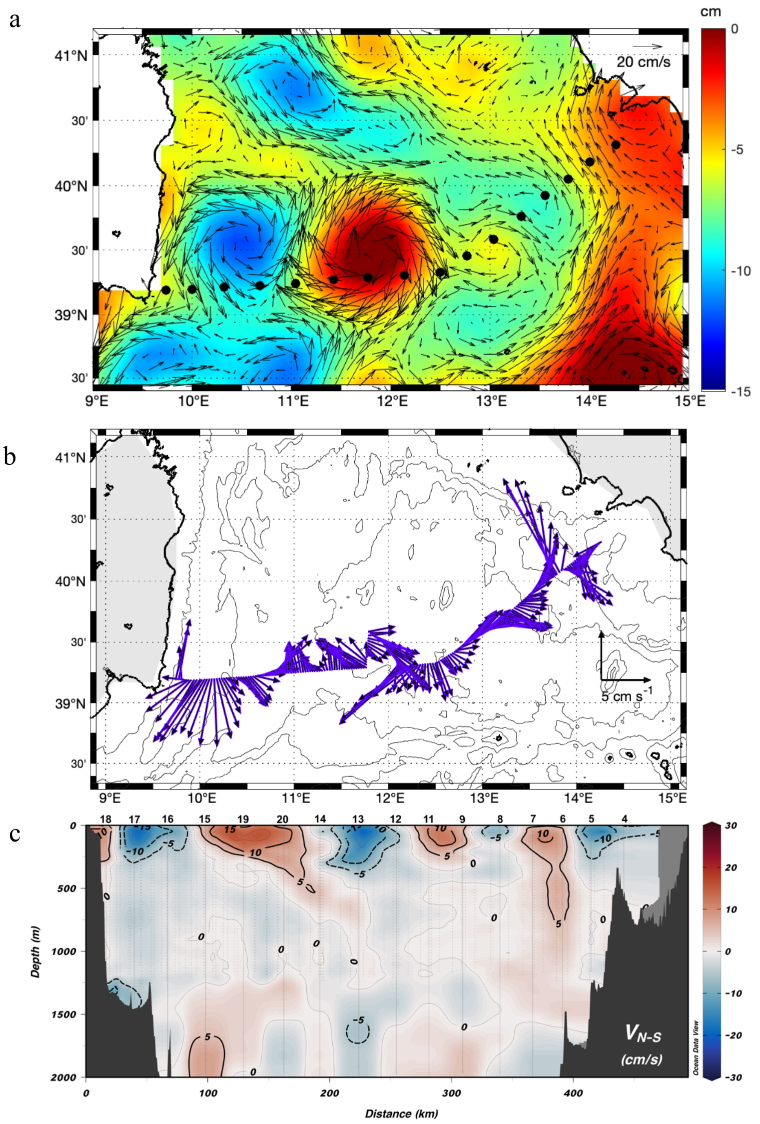

Figure 3: (a) Mean absolute dynamic topography (in cm) and surface geostrophic currents derived from the daily product during the period of the cruise (14–16 March 2020). The product

a supprimé: L

a supprimé: ¶

is the European Seas Gridded L 4 Sea Surface Heights and Derived Variables product, interpolated to a 3.75 arcmin grid, provided by the Copernicus Marine Environment Monitoring Service (CMEMS). (b) Stick plot of vertically averaged S-ADCP currents between 21 m and 1200 m along the ship's route across the basin, (c) Meridional component of combined S-ADCP and L-ADCP currents between the 21 and 2000 m depth for the PERLE-3 cruise.

The estimated vertical velocities for the layer between the surface and 2000 m depth (Fig. 4) are between -15 and 15 mm s^{-1} with a rms of 4 mm s^{-1}. There was no significant spatial variation in vertical velocities, apart from greater vertical shear in the first 300 m of the water column on either side of the eddy at around 12°E.

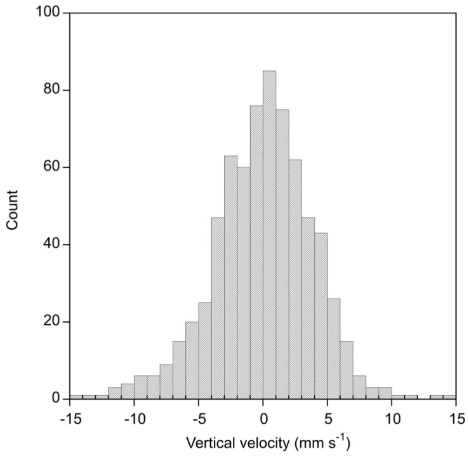

Figure 4: Histogram of the vertical velocities between 20 and 2000 m depth estimated form the L-ADCP measurements for all the stations during the PERLE 3 cruise.

3.1.3 Turbidity, large particle abundance and Junge index

The beam attenuation coefficient, an indicator of the abundance of small particles (Fig. 5a) is highest in the surface layer and along the continental slope on both sides of the basin. The tongue of turbid water that descends to 500–600 m in the western half of the basin is associated with the downward movement of water around the anticyclonic eddy.

Coarse particles observed with the UVP (Fig. 5b) are most abundant along the continental slope and between 400 and 900 m depth throughout the basin. The subduction effect of the anticyclonic eddy is also evident in the abundance of large particles.

a

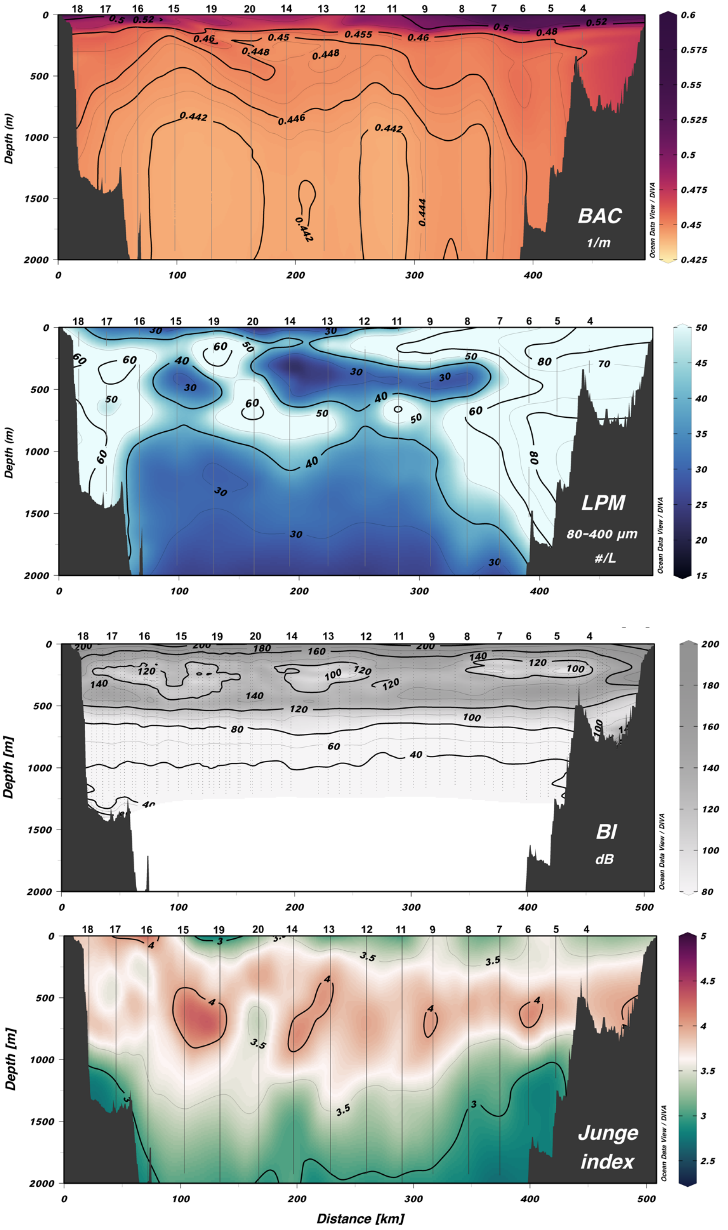
BAC
1/m
LPM
80–400 µm
#/L
BI
dB
Junge
index
Depth (m)
Depth [m]
Distance [km]
Ocean Data View / DIVA

d

Figure 5: Cross-basin section of (a) beam attenuation coefficient, (b) total large particle abundances, (c) backscatter index for the PERLE-3 cruise, and (d) Junge index.

An accumulation of large reflectors between 200 and 500 m depth is clearly visible on the 38 kHz ADCP echo intensity (Fig. 5c). It corresponds to the deep scattering layer formed by the micronekton (small mesopelagic fishes, crustaceans, and cephalopods) (Kapelonis et al., 2023; Peña, 2024) . Its fragmentation into "tongue" of lower intensity between 200-300 m is related to the diel vertical migrations (upward motion) of part of the organisms at night.

a mis en forme : Police :Non Italique, Non souligné, Anglais (E.U.)

a mis en forme : Non Surlignage

a mis en forme : Non Surlignage

The Junge index (Fig. 5d), estimated from UVP data, shows an intermediate maximum – indicating the preponderance of smaller particles over coarser ones – between 400 and 1000 m, below the deep scattering layer. Below 1000 m, the index decreases by one unit to 2000 m depth, indicating a decrease in the relative abundance of smaller particles compared to coarser particles. This decrease is more pronounced on the continental slope.

a supprimé: relative

a supprimé: and below deep eddies

3.2 Hydrological features of thermohaline staircases

3.2.1 Attributes of staircase station vs. "non-staircase" station

In this section we describe the vertical distribution of physical, dissolved and particulate parameters at station 20, which shows virtually no significant staircase (Fig. 6), and station 09 which shows marked staircases between 700 and 1700 m (Fig. 7).

At station 20, the vertical profiles of most variables exhibit relatively uniform characteristics between 800 m and 1070 m depth. At 1070 m, a homogeneous layer of approximately 70 m thickness is observed, immediately succeeded by a pronounced density interface. The water column structure below this interface demonstrates increased variability, characterized by minor step-like features in the measured parameters.

The profiles of physical variables at station 09 show a series of steps starting at 750 m depth. Density steps result in thin interfaces (about 9–73 m) and density variations of a few thousandths of a kg m^{-3}. The thickness of the mixed layers varies between 10 and 230 m and increases significantly below 1000 m. The profiles of the biogeochemical variables also show step-like profiles, with larger gradients corresponding to the density steps and nearly homogeneous concentrations in the mixed layers between each step. This is clearly visible for dissolved elements (oxygen, nitrate) and small particle concentration (beam attenuation coefficient). The effect of the density steps on the abundance of coarser material is less obvious due to the variability of the measurements, but it still appears that the total abundance decreases significantly below each step. It is noteworthy that the decrease in the Junge index between 700 and 1600 m is greater for station 9 with staircase steps, of the order of one unit, than for station 20, which is more irregular and of the order of 0.2 units.

a supprimé: /

a mis en forme : Exposant

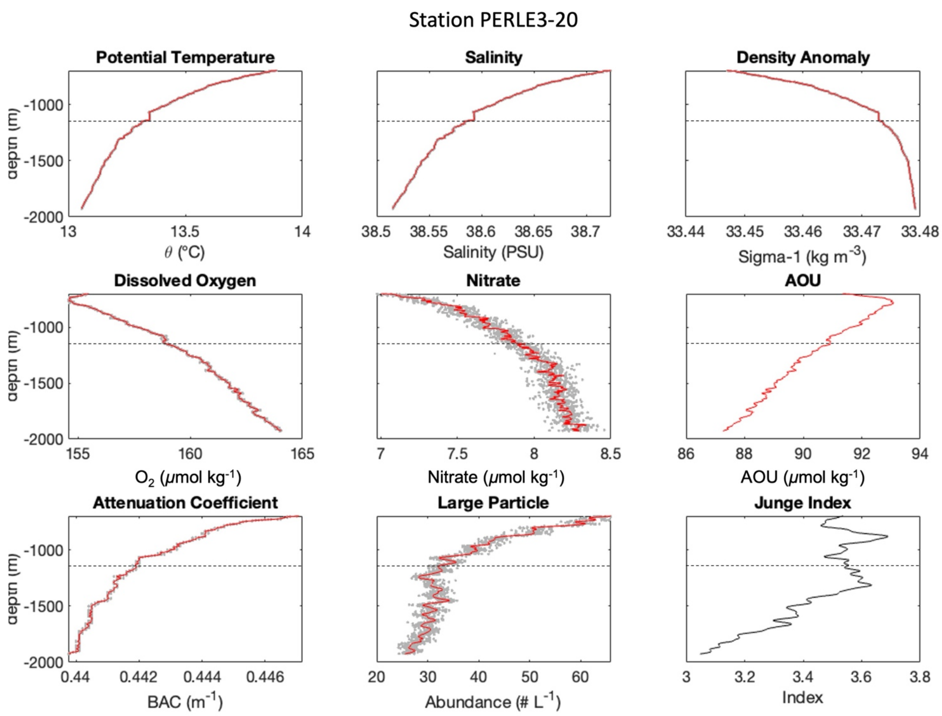

Figure 6: Profiles of potential temperature, salinity, potential density anomaly (top row) and dissolved oxygen, nitrate, and apparent oxygen utilization (AOU) (middle row), beam attenuation coefficient, large particle abundance between 80 and 400 μm, and Junge index (bottom row) between 700 and 1700 m deep for station PERLE3-20. The grey dots are the data binned at 1-metre intervals and the solid red line indicates the smoothed profile. The horizontal dashed line indicates the base of the main density interface. See station position in Fig. 1.

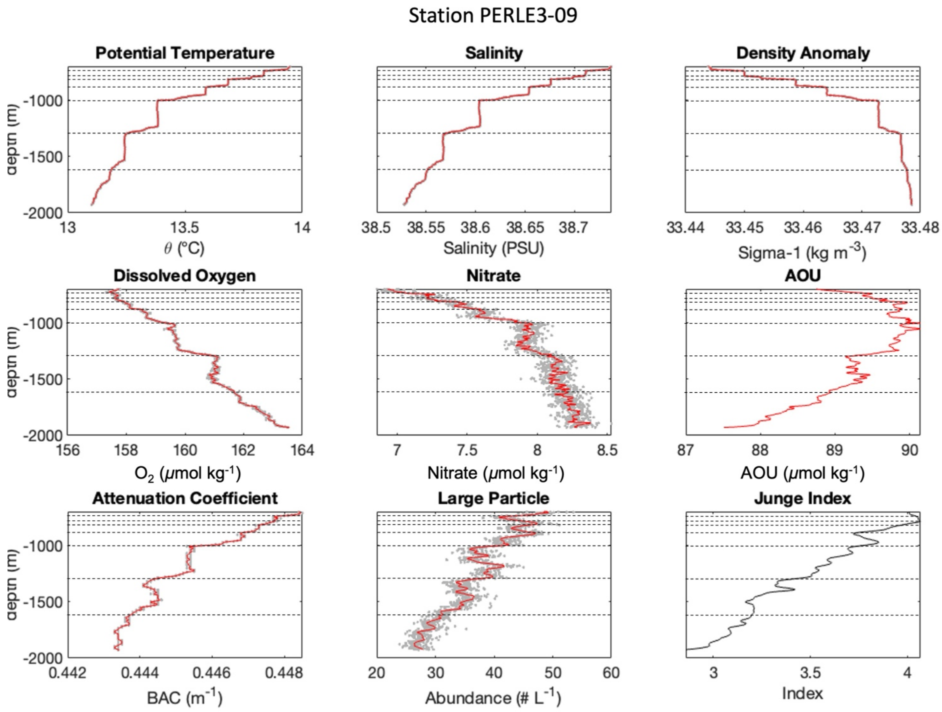

Fig. 7: Profiles of potential temperature, salinity, potential density anomaly (top row) and dissolved oxygen, nitrate, and apparent oxygen utilization (AOU) (middle row), beam attenuation coefficient, large particle abundance between 80 and 400 µm, and Junge index (bottom row) between 700 and 1600 m deep for station PERLE3-09. The grey dots are the data binned at 1-metre intervals and the solid red line indicates the smoothed profile. Major density steps are delineated by horizontal grey lines. The horizontal dashed lines indicate the base of the main density interfaces. See station positions in Fig. 1.

3.2.2 Positioning and persistence of main staircases

The transition zone between the EIW and the TDW thus provides the right conditions (warmer and saltier water mass overlying a colder and less saline water mass) for salt fingers. The thermohaline gradients from the profiles collected during the cruise and from the profiling float allowed us to identify the main stepped structures in the Tyrrhenian Basin (Fig. 8).

During the PERLE-3 cruise, distinct thermohaline staircases are observed between 600 and 2000 m depth, primarily in the central region of the basin (Fig. 8a). These staircases are

a supprimé: L

a supprimé: salty

a supprimé: the double diffusion phenomenon by

a supprimé: analysis of the

a supprimé: and position

notably absent in two areas: near the western slope of the basin and beneath the deep anticyclonic eddy located at about 12° E. The absence of staircases extends to 1000 m depth beneath this eddy.

a supprimé: During the PERLE3 cruise, the staircases develop clearly between 600 and 2000 m depth, mostly in the centre of the basin (Fig. 8a). Staircases are absent under the deepest eddy (about 12° E). Staircases are absent near the western slope and below the anticyclonic eddy at about 12° E down to 1000 m depth.

The temporal evolution of the staircase in the centre of the basin, as seen by the profiling float between July 2018 and March 2020, underscores that these structures, particularly at depths greater than 1000 m, are relatively stable and have been maintained for several years (Fig. 8b).

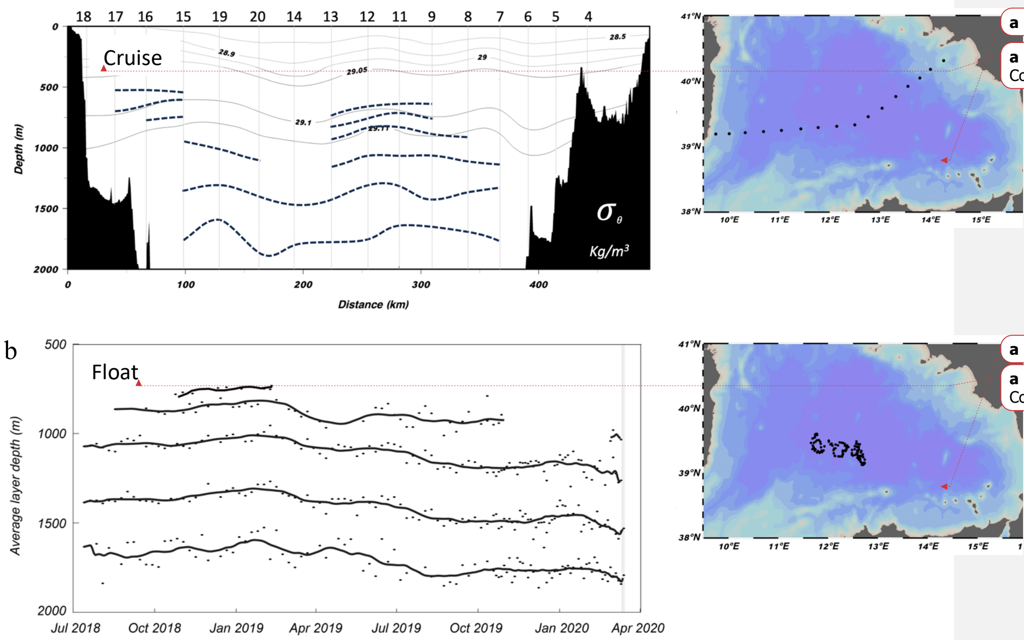

a mis en forme : Retrait : Gauche : 0,12 cm

a mis en forme : Police :(Par défaut) +Corps (Calibri), 12 pt, Couleur de police : Texte 1

a mis en forme : Retrait : Gauche : 0,1 cm

a mis en forme : Police :(Par défaut) +Corps (Calibri), 12 pt, Couleur de police : Texte 1

a mis en forme : Retrait : Gauche : 0,25 cm

Figure 8: (a) depth of the main thermohaline staircases across the basin during the PERLE-3 cruise and (b) temporal evolution of the staircases in the centre of the basin as seen by the profiling float between July 2018 and March 2020. The shaded band indicates the campaign period. The position of the stations and the trajectory of the profiling float are shown on the maps on the right.

4. Discussion

4.1 Circulation and thermohaline staircases

a supprimé: Characteristics and development conditions of the notable staircase

The hydrodynamic patterns observed during the PERLE-3 cruise are consistent with the established understanding of winter circulation in the southern Tyrrhenian Sea (Rinaldi et al., 2010; Iacono et al., 2013; Iacono et al., 2021). The winter circulation in this region is primarily driven by wind forces, resulting in a vigorous cyclonic flow that encompasses the entire Tyrrhenian Basin and persistent mesoscale eddy structures. The observed anticyclonic gyre between 12°E-13°E and 39°N-40°N, and the cyclonic circulation between Sardinia and Sicily, corroborate the findings of previous studies.

Our observations in the Tyrrhenian Sea between the surface and 2000 m show some well-defined thermohaline staircase structures associated with salt fingers. The observed thermohaline staircases occur mainly in the centre of the Tyrrhenian Basin and are less defined on the continental slope at both ends of the section. These latter regions are the ones that contain the cyclonic boundary circulation that entrains the core of the EIWs originating from the Strait of Sicily.

These results are consistent with those of Zodiatis and Gasparini (1996) from ship observations, of Buffett et al. (2017) from seismic observations, and Taillandier et al. (2020) from profiling float observations, who showed that the staircases with the most distinct step-like gradients appear in the centre of the basin, while they become less evident towards the boundaries and the bottom. They linked this change to increased vertical motions that prevent diffusive convection and staircase formation because the internal wave field and current shear are stronger near the boundaries. Similarly, Durante et al. (2021) found that internal gravity wave-induced mixing can modulate staircase structures in the basin interior. In addition, Yang et al. (2024) used seismic data from the Caribbean to show that mesoscale eddies can generate turbulent mixing that significantly perturbs thermohaline staircase structures down to depths of 750 m. These eddies appear to generate vertical shear and instability, particularly at their periphery, leading to the disruption of thermohaline staircases. Our observations show an absence of staircases up to 1000 m deep beneath the anticyclonic eddy centered at 12°E. While this co-occurrence does not establish causality, and in the absence of direct turbulence measurements, the potential disruptive effect of this eddy on staircase formation warrants consideration. This observation is consistent with the emerging understanding of the dynamic interplay between mesoscale features and fine-scale thermohaline structures in the ocean interior.

The persistence of thermohaline steps observed below 1000 m depth, as evidenced by both float measurements and cruise data in the basin's central region, also corroborates previous observations that have highlighting the stability of these structures in the basin interior. These step-like features have been documented to maintain their integrity over temporal scales ranging from years (Zodiatis and Gasparini, 1996; Falco et al., 2016; Taillandier et al., 2020) to decades (Durante et al., 2019) and show strong lateral coherence, sometimes reaching several hundred kilometres (Buffett et al., 2017). The size of the region occupied by thermohaline staircases is controlled by the competition between turbulent mixing and double diffusion. Ferron et al. (2017) measured very low microstructure derived dissipation rates in the southwestern part of the Tyrrhenian. This low turbulence plays a crucial role in allowing double-diffusive mixing to dominate transport processes, promoting the development and persistence of thermohaline staircases.

a mis en forme : Français

Code de champ modifié

a mis en forme : Anglais (E.U.)

a supprimé: A large part of the oceanic regions are suitable for the process of double diffusion and salt fingering, but it clearly develops only in some of them, especially in the Mediterranean. Meccia et al. (2016) have shown that about 50% of the Mediterranean Sea is favourable for double diffusion processes, with the Tyrrhenian, Ionian, and southwestern Mediterranean basins being most susceptible to salt fingering, and the strongest processes potentially occurring in the deep waters of the Tyrrhenian Sea.

a supprimé: , while observations made during the PERLE cruises in the Ionian Sea and Levantine Basin do not show any particulate structures associated with salt fingers

a supprimé: L

a supprimé: more diffuse

a supprimé: diffuse

a supprimé:

a mis en forme : Anglais (E.U.)

a mis en forme : Anglais (E.U.)

a mis en forme : Anglais (E.U.)

a mis en forme : Anglais (E.U.)

a mis en forme : Anglais (E.U.)

The subsequent sections provide a detailed examination of how these persistent, well-developed thermohaline staircases may influence particulate matter dynamics, specifically addressing their impact on sedimentation processes (§ 4.2) and the degradation of suspended particles (§ 4.3). This analysis aims to investigate the complex interactions between small scale physical oceanographic features and biogeochemical cycles in the deep marine environment.

4.2 Impact of staircases on the distribution and settling of particulate matter

The slope of the Junge-type particle size spectrum has been shown to be a valid first-order description of the particle size distribution, particularly for the study of size-dependent processes such as particle sinking (Guidi et al., 2009). In our case, the observed abundance of coarse particles and the slope of the particle size spectrum are greatest in the deep scattering layer between 400 and 800 m (Fig. 5). Deeper down to 2000 m, both the total particle abundance and the slope of the size spectrum decrease, indicating that the contribution of coarser particles to the particle population increases with depth. Similar results regarding the size distribution of smaller particles in the Tyrrhenian Basin were obtained by (Chaikalis et al., 2021) during the trans-Mediterranean cruise in March 2018 using an in-situ laser scattering and transmissometry instrument (LISST-Deep). In their study, they considered the size range between 5.6 and 92.6 µm, complementary to that measured with the UVP. Their stations show similar particle distribution size with depth below the surface layer (>150 m), with an intermediate maximum at about 400–500 m depth and a steady decrease to 2000 m depth. Such an evolution of the abundance and particle size distribution is generally considered to be the result of aggregation, with smaller particles agglomerating to form larger ones, a common process in the ocean (McCave, 1984).

The overall diminution suspended particles abundance, concurrent with an augmentation of the coarse fraction, is evident not only on a macroscale throughout the water column beneath the Eastern Intermediate Waters (EIWs), but also manifests on a microscale (spanning several decameters) within the thermohaline staircases. The influence of density steps on the vertical distribution of particle abundance and size is illustrated through an examination of three distinct interfaces, situated at different stations and depths ranging from 700 to 1400 m, i.e. station 08 (Fig. 9), station 11 (Fig. 10), and station 09 (Fig. 11). These interfaces, characterized by thicknesses varying between 20 and 75 m, exhibit density variations of 3 to 5 × 10^{-3} kg m^{-3}.

These examples show a significant reduction in the abundance of fine particles, as evidenced by transmissometry (BAC) measurements, across each interface. For coarse particles detected by UVP, despite measurement variability, the change in abundance across the interface varies according to particle size. At stations 08 (Fig. 9) and 11 (Fig. 10), a slight decrease in abundance is observed for the smallest size fraction (80.6-161 µm), while minimal variation is noted for intermediate sizes (161-256 µm), and an increase is evident for the largest particles (> 256 µm). At station 08, the Junge index exhibits a clear decrease across the density interface. The signal is less pronounced at station 11, where the index decreases at the interface's upper boundary but shows a localized increase at its base. For the interface at station 09 (Fig. 11), all parameters — turbidity, abundance across different size fractions, and the Junge index —

a supprimé: Durante et al. (2021) suggested that mixing induced by internal gravitational waves can modulate the staircase structure. Our observations show that the presence of significant staircase structures down to 2000 m can also be influenced by mixing induced by cyclonic eddies present in the basin. When the vertical extent of these eddies reaches depths deeper than the LIW (i.e. about 500 m), the intensity and variability of the currents in the transition zone between the LIW and the TDW visibly alter the development of the staircases. These observations confirm that, even within the basin, step structures appear to develop preferentially in areas of weak horizontal and vertical currents. However, the modification by eddies would be episodic and would hardly affect the lower part of the salt finger region, as several studies show that the central Tyrrhenian thermohaline steps observed in the heart of the basin interior are quite stable and can persist for years(Zodiatis and Gasparini, 1996)(Falco et al., 2016) (Taillandier et al., 2020) to decades (Durante et al., 2019). ¶

a supprimé: µ

a supprimé: Their

a supprimé: distribution size with depth

a supprimé: distribution

a mis en forme : Exposant

a supprimé: on both sides of

decrease across the interface. These depth-dependent variations provide strong evidence that these density interfaces exert a significant influence on particle abundance and size distribution.

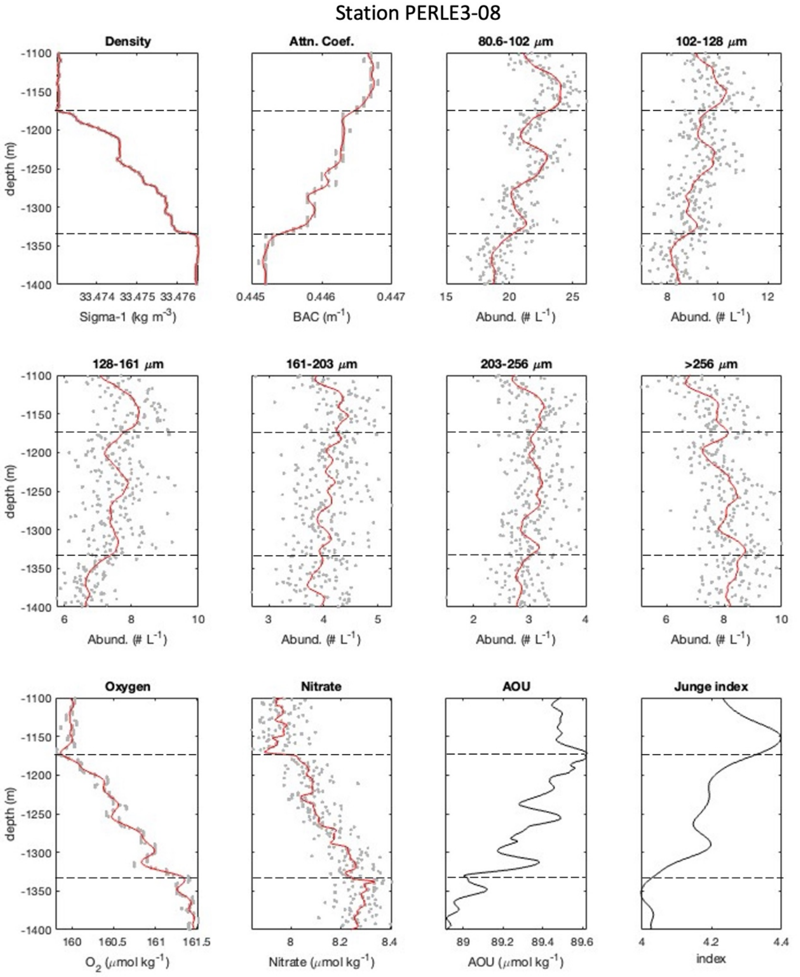

Figure 9: Profiles of potential density anomaly, beam attenuation coefficient, large particle abundances for the first five size classes and for all sizes>256 μm of the UVP, dissolved oxygen, nitrate, apparent oxygen utilization (AOU), and Junge Index between 1100 and 1400 m deep for station PERLE3-08. The top and base of the interface is delimited by dashed lines.

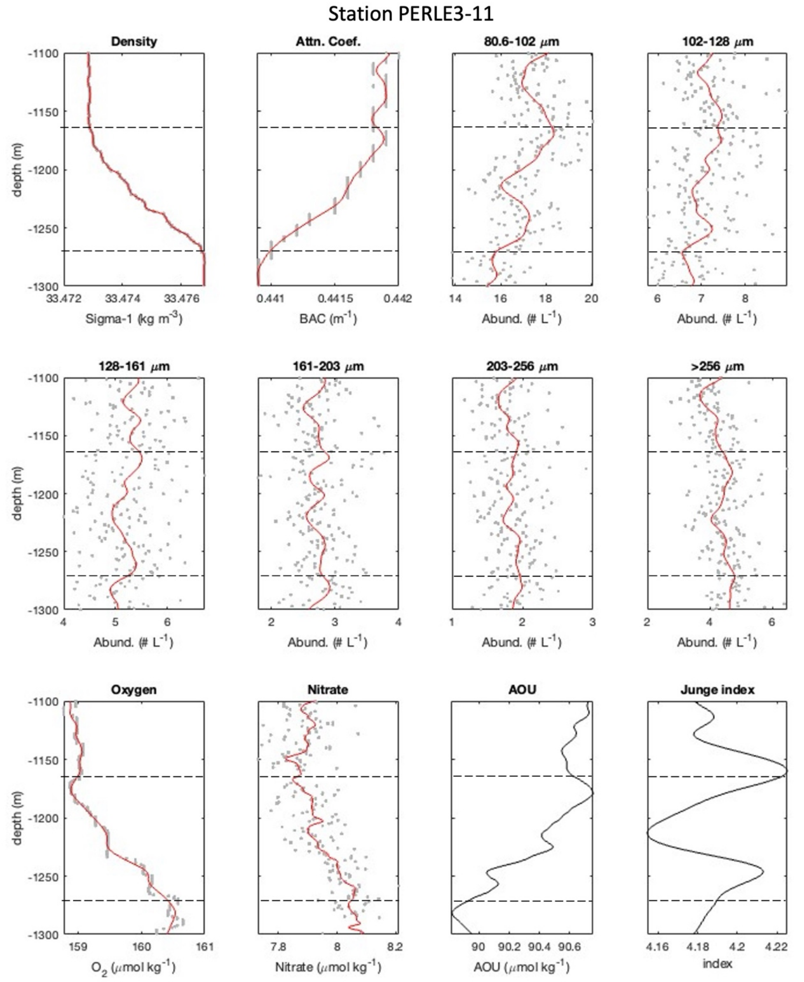

Figure 10: Profiles of potential density anomaly, beam attenuation coefficient, large particle abundances for the first five size classes and for all sizes>256 µm of the UVP, dissolved oxygen, nitrate, apparent oxygen utilization (AOU), and Junge Index between 1100 and 1300 m deep for station PERLE3-11. The top and base of the interface is delimited by dashed lines.

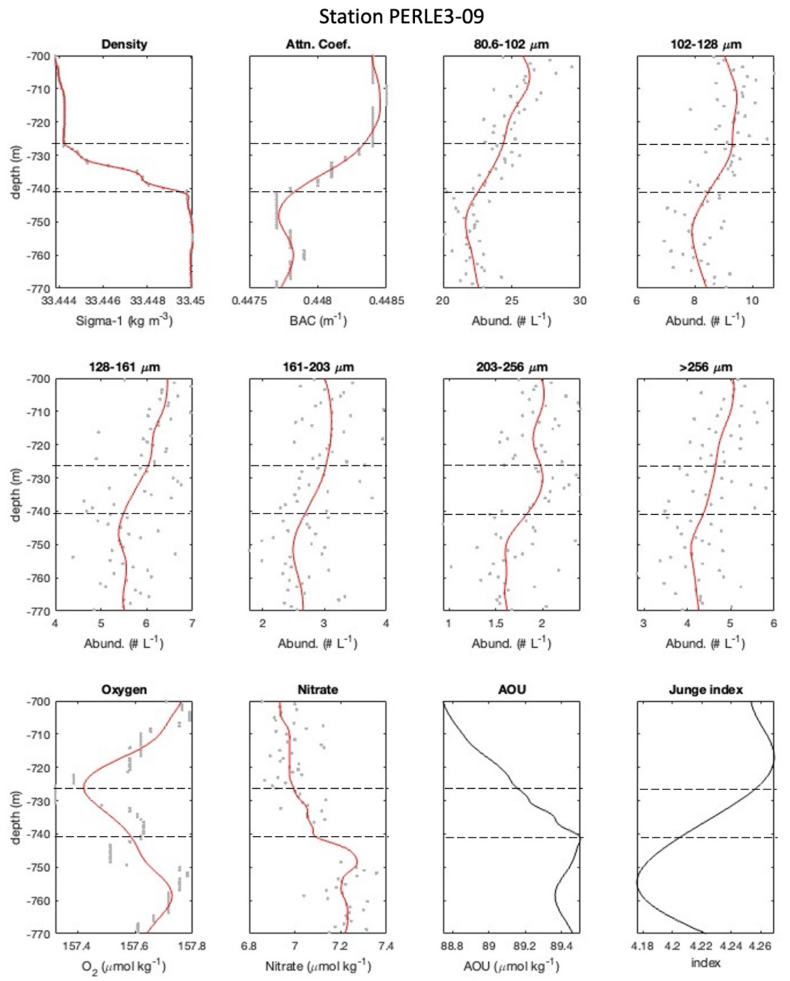

Figure 11: Profiles of potential density anomaly, beam attenuation coefficient, large particle abundances for the first five size classes and for all sizes>256 μ m of the UVP, dissolved oxygen, nitrate, apparent oxygen utilization (AOU), and Junge Index between 700 and 770 m deep for station PERLE3-09. The top and base of the interface is delimited by dashed lines.

Based on laboratory and modelling experiments in the literature, strong density interfaces are known to cause particle retention and promote aggregation. According to (Doostmohammadi and Ardekani, 2015), density interfaces can induce preferential retention of fine, slow-sinking particles compared to larger particles, and can therefore promote the

a supprimé: ¶

formation of clusters of fine particles, which can then aggregate. This retention phenomenon can also act on coarse particles, which are often formed by high porosity aggregates. According to Kindler et al. (2010), large porous particles whose effective density is close to that of ambient water are much more dependent on transition zones and large accumulations of porous particles can occur at interfaces due to their less dense water transport, which is also conducive to aggregation. In our case, the density difference at the interface between two staircases are really weak (a few thousandths of kg/m^3) and despite the measurement uncertainty of the particle abundances, the results suggest that these interfaces have an effect on the size distribution – through retention and aggregation – of the settling particles. The larger particles, which are generally denser and have higher settling velocities, are not affected by the change in water density.

In addition, convection phenomena in the mixed layers sandwiching the density interfaces are likely to even out the concentration of slowly sinking particles (especially the finest and most numerous). The estimated vertical velocities of the current, on the order of a few mm s^{-1}, are likely to alter the settling of particles, helping to homogenize their abundance with depth and increase their residence time in each layer.

4.3 Potential impact of staircases on the biogeochemical activity

The vertical export of organic particles to the deep ocean is a crucial component of the oceanic carbon cycle, with flux decreasing significantly (>70%) in the mesopelagic zone (100-1000 m depth). Several biogeochemical processes are responsible of the reduction of this flux and particle lability decrease with depth. Briggs et al. (2020) suggest that particle fragmentation could account for approximately half of the observed particle loss in the mesopelagic zone. Additionally, remineralization by heterotrophic respiration and enzymatic solubilization both by free-living and particle-attached microbes play a key role in particle degradation (Karl et al., 1988; Collins et al., 2015). It is also well known that marine snow aggregates act as hotspots for microbial activity, hosting diverse communities of bacteria, protozoans, and other microorganisms. Particle-attached microbial community evolves with depth, due to evolution of the initial attached community rather than de novo colonization, detachment or grazing as the marine snow sinks (Thiele et al., 2015). These communities are often orders of magnitude more concentrated and active than those in the surrounding water, leading to intense localized degradation and remineralization of organic matter (Kiørboe, 2001; Baumas and Bizic, 2024).

The presence of thermohaline staircases appears to affect the sedimentation pattern of particles; promoting particle retention and aggregation, increasing the time particles spend in the water column. These structures also create distinct microenvironments with gradients of oxygen and nutrients, which are believed to be the result of the degradation of particulate organic. This effect is illustrated for three separate interfaces in figures 9 to 11. It can be then hypothesized that the increase in particle residence time favors the remineralization process, which releases nutrients while consuming dissolved oxygen through heterotrophic respiration. Depending on the conditions and with a sufficiently long stability period, these activities can lead to localized oxygen depletion and an increase in AOU. In our data, this effect is clearly observed in the shallower staircases, between 750 and 900 m, at station 09 (Fig. 11, bottom row). For deeper interfaces for stations 08 and 11, at around 1200 m (Figs. 9 and 10, bottom

a supprimé: staircase density interfaces
a supprimé: measured
a supprimé: at
a supprimé: ±
a supprimé: /s
a supprimé: equalise
a mis en forme : Exposant
a mis en forme : Non Surlignage
a supprimé: At station 20 (fig. 6), the lack of staircase structures and density interfaces results in relatively uniform sedimentation of particulate matter and relatively homogeneous biogeochemical processes throughout the water column. As particles descend into the deep ocean, they undergo a progressive but overall constant mineralization process by bacteria (Ghiglione et al., 2009). In contrast, stations with staircase structures show distinct layered profiles for dissolved oxygen and nitrate (figs. 10 and 11). These staircases facilitate the retention and aggregation of sinking particulate matter, which is critical for the mineralization and transformation of organic matter in the water column (Wakeham and Lee, 1993). This remineralization process releases additional nutrients and consumes oxygen, potentially leading to localized oxygen depletion or an increase in Apparent Oxygen Utilization (AOU), particularly evident in the shallow staircases between 750 and 900 m at station 9 (Fig. 11). At the deeper interface around 1300 m (Fig. 12), the increase in AOU may be masked by a stronger vertical oxygen gradient. These interfac ... [1]
a mis en forme : Police :(Par défaut) Times New Roman, 12 pt
a mis en forme : Police :(Par défaut) Times New Roman, 12 pt
a mis en forme : Anglais (E.U.)
Code de champ modifié
a mis en forme : Police :(Par défaut) Times New Roman, 12 pt, Anglais (E.U.)
a mis en forme : Police :(Par défaut) Times New Roman, 12 pt
a mis en forme : Police :(Par défaut) Times New Roman, 12 pt
a mis en forme : Anglais (E.U.)
a mis en forme : Police :(Par défaut) Times New Roman, 12 pt
a supprimé: appears
a mis en forme : Police :(Par défaut) Times New Roman, 12 pt
a mis en forme : Police :(Par défaut) Times New Roman, 12 pt
a mis en forme : Police :(Par défaut) Times New Roman, 12 pt
a mis en forme : Police :(Par défaut) Times New Roman, 12 pt
a mis en forme : Police :(Par défaut) Times New Roman, 12 pt
a mis en forme : Police :(Par défaut) Times New Roman, 12 pt
a mis en forme : Police :(Par défaut) Times New Roman, 12 pt

row), the increase in AOU and the potential accumulation of nitrate are masked by a stronger vertical oxygen gradient and higher nutrient concentrations compared to shallower depths. Moreover, biological activity within these deeper staircases is also reduced due to the decreased lability of organic matter with increasing depth (Ghiglione et al., 2009; Karl et al., 1988).

The persistence of these staircase structures over long periods of time leaves sufficient time for significant biogeochemical transformations to occur. Arístegui et al. (2009) and Nagata and Kirchman (1997) showed that in deep marine environments, the degradation kinetics of organic matter, which vary according to temperature, oxygen availability, and microbial composition, can range from a few days to several months. This can lead to the local accumulation of nitrates, creating pockets of higher concentration and intensifying vertical double diffusive nitrate fluxes toward upper layers. However, observing these accumulations with the present resolution and precision remains challenging. Taillandier et al. (2020) already showed that the thermohaline staircases in the Tyrrhenian Sea significantly influence the biogeochemical dynamics by contributing to the nitrate enrichment of the EIW through diffusion. They estimated upward nitrate fluxes (assuming weak turbulent diapycnal diffusivity) in the transition zone between 400 and 2000 m depth to be about 4 µmol m^{-2} d^{-1} using the salt diffusivity formulation of Radko and Smith (2012) based on the density ratio ($R_\rho = \alpha \times \partial\theta/\partial z / \beta \times \partial S/\partial z$), where α and β are the thermal expansion and haline contraction coefficients of seawater, respectively, and the molecular diffusivity of heat is $k_T = 1.4 \times 10^{-7}$ m^2 s^{-1}. We calculated nitrate diffusive fluxes, in assuming weak turbulent diapycnal diffusivity, at each interface using the same formulation. The nitrate flux (F_{NO3}) can be expressed as:

$$F_{NO3} = K_{sf} \times \partial C_{NO3}/\partial z = k_T \times R_\rho \times (135.7/ (R_\rho - 1)^{1/2} - 62.75) \times \partial C_{NO3}/\partial z$$

where K_{sf} is the salt-fingering diffusivity of nitrate and $\partial C_{NO3}/\partial z$ the vertical gradient in nitrate concentration.

At station 09, the diffusive nitrate flux was assessed for each depth step between 600 and 1600 m (Fig. 12). Fluxes ranged from 3.8 µmol m^{-2} d^{-1} at the deepest depth (1254 m) to 19.1 µmol/m²/d for the three shallower depths (728 to 870 m). The fluxes at the interfaces are therefore stronger than the overall flux estimated by Taillandier et al. (2020) for the 400-2000 m depth range. Fluxes at interfaces are the major contributor to the total nitrate flux. In agreement with our estimation of double diffusive upward nitrate flux, Durante et al. (2021) estimated that heat and salt fluxes are more pronounced in the upper part of the staircases zone (700 m – 1600 m) but decrease below 1800 m, reaching a minimum near the base of the staircases.

a mis en forme ... [2]
a mis en forme ... [3]
a mis en forme ... [4]
a mis en forme ... [5]
a supprimé: ¶
a mis en forme ... [6]
a mis en forme ... [7]
a supprimé: L
a supprimé: /
a supprimé: ²/
a mis en forme ... [8]
a mis en forme ... [9]
a mis en forme ... [10]
a mis en forme ... [11]
a supprimé: –
a supprimé: –
a supprimé: –
a mis en forme ... [12]
a mis en forme ... [13]
a mis en forme ... [14]
a mis en forme ... [15]
a mis en forme ... [16]
a supprimé: /s
a supprimé: Based on this study,
a supprimé: w
a supprimé: fluxes
a mis en forme ... [17]
a mis en forme ... [18]
a mis en forme ... [19]
a mis en forme ... [20]
a mis en forme ... [21]
a mis en forme ... [22]
a mis en forme ... [23]
a mis en forme ... [24]
a mis en forme ... [25]
a mis en forme ... [27]
a mis en forme ... [26]
a supprimé: ¶
a mis en forme ... [28]
a mis en forme ... [29]
a mis en forme ... [30]
a supprimé: that
a mis en forme ... [31]
a mis en forme ... [32]
a supprimé: It is conceivable that the release of additional ... [33]

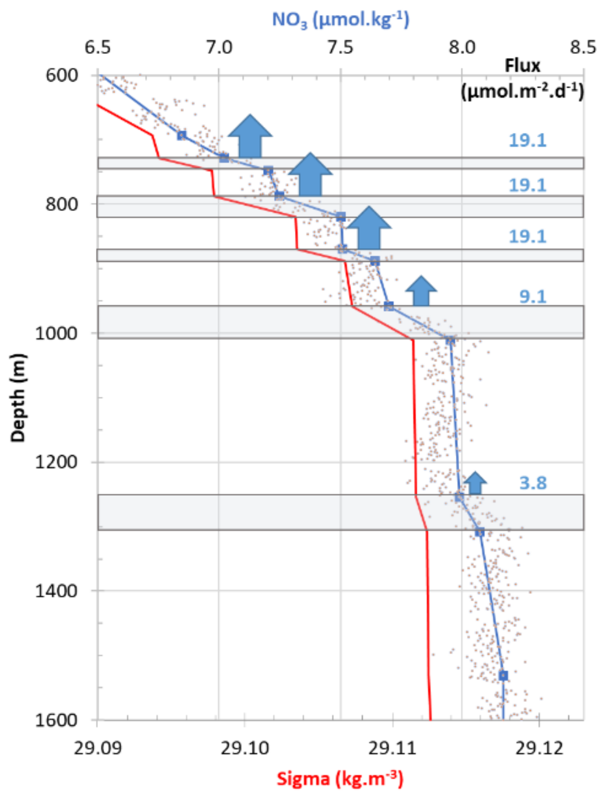

Figure 12: Estimated double diffusive nitrate fluxes across each interface (annotated in blue and expressed in µmol/m²/d) from station 9. The blue arrows indicate the direction of the flux and the sizes are proportional to the intensity. In red: the vertical profile of the specific volume anomaly (σ_θ in kg m^{-3}) delimiting homogeneous and gradient zones. The grey points correspond to nitrate measurements by the SUNA, while the blue squares are the values averaged over 1 m for each point at the upper and lower interfaces, and used to calculate the nitrate gradient in the shaded areas.

a mis en forme : Non Surlignage

a supprimé: *at the interfaces of each gradient zone characterizing a staircase step…*

a supprimé: */*

a mis en forme : Exposant

a mis en forme : Non Surlignage

a supprimé: *making it possible*

5. Conclusion

This study examines the effect of observed weakly stepped density gradients induced by salt fingering on the distribution and fluxes of particulate and dissolved elements. While the effect of density steps on particle settling has been well studied experimentally and demonstrated for strong density gradients in natural environments (i.e. buoyant river plumes

a supprimé: observations of

and pycnocline), this is the first time, to our knowledge, that this effect has been identified for steps with the extremely low-density gradients that exist in the deep ocean.

a supprimé: .

In the Tyrrhenian Sea, the interface between the warm and saline intermediate waters (EIW) and the colder and less saline deep waters (TDW) presents thermohaline conditions favourable to the development of significant salt fingering staircases. These structures are predominantly observed in regions characterized by minimal hydrodynamic activity, situated in the interior of the basin, distanced from boundary influences, and beneath the depth of influence of mesoscale eddy dynamics. In addition, the study shows that the thermohaline staircases in the central region of the Tyrrhenian Basin are remarkably stable over time, persisting for several years.

a supprimé: L

These results underscore the complex interplay between thermohaline staircases and sedimentary fluxes, dissolved matter distribution, and ecological and biogeochemical processes in deep marine environments. The presence of thermohaline staircases appears to have a significant influence on the distribution of particulate and dissolved matter. Profiles of particle abundance resolved down to a few hundred microns, or profiles of dissolved substances such as oxygen and nitrate, tend to mirror the step-like structure observed in the density profiles. Thermohaline staircases create distinct density interfaces that act as physical barriers, slowing the descent of particles. The retention of near-floating particles at density interfaces increases their residence time, promotes particle aggregation and, incidentally, allows the larger particles thus formed to cross the density interface. At the same time, the staircases influence the concentration of nutrients (such as nitrate) and dissolved oxygen levels, thereby potentially affecting microbial activity and nutrient cycling within these interfaces. The retention of part of the particulate material at the density interfaces allows the mineralization of organic matter, contributing to nitrate enrichment and increasing the upward diapycnal diffusive fluxes of oxygen and nitrate. Ecologically, it is assumed that these staircases can play a crucial role in promoting diverse habitats and influencing the lability of organic matter and the nutrient distribution and fluxes.

a supprimé: significantly

Such findings underscore the importance of fine-scale physical structures in shaping the biogeochemical landscape of the ocean interior. and emphasizes the need for further research to fully understand their implications for marine ecosystems.

References

Arístegui, J., Gasol, J.M., Duarte, C.M., Herndld, G.J., 2009. Microbial oceanography of the dark ocean's pelagic realm. Limnology & Oceanography 54, 1501–1529. https://doi.org/10.4319/lo.2009.54.5.1501

Baumas, C., Bizic, M., 2024. A focus on different types of organic matter particles and their significance in the open ocean carbon cycle. Progress in Oceanography 224, 103233. https://doi.org/10.1016/j.pocean.2024.103233

Briggs, N., Dall'Olmo, G., Claustre, H., 2020. Major role of particle fragmentation in regulating biological sequestration of CO_2 by the oceans. Science 367, 791–793. https://doi.org/10.1126/science.aay1790

Buffett, G.G., Krahmann, G., Klaeschen, D., Schroeder, K., Sallarès, V., Papenberg, C., Ranero, C.R., Zitellini, N., 2017. Seismic Oceanography in the Tyrrhenian Sea: Thermohaline Staircases, Eddies, and Internal Waves. JGR Oceans 122, 8503–8523. https://doi.org/10.1002/2017JC012726

Chaikalis, S., Parinos, C., Möbius, J., Gogou, A., Velaoras, D., Hainbucher, D., Sofianos, S., Tanhua, T., Cardin, V., Proestakis, E., Amiridis, V., Androni, A., Karageorgis, A., 2021. Optical Properties and Biochemical Indices of Marine Particles in the Open Mediterranean Sea: The R/V Maria S. Merian Cruise, March 2018. Front. Earth Sci. 9, 614703. https://doi.org/10.3389/feart.2021.614703

Collins, J.R., Edwards, B.R., Thamatrakoln, K., Ossolinski, J.E., DiTullio, G.R., Bidle, K.D., Doney, S.C., Van Mooy, B.A.S., 2015. The multiple fates of sinking particles in the North Atlantic Ocean. Global Biogeochemical Cycles 29, 1471–1494. https://doi.org/10.1002/2014GB005037

Doostmohammadi, A., Ardekani, A.M., 2015. Suspension of solid particles in a density stratified fluid. Physics of Fluids 27, 023302. https://doi.org/10.1063/1.4907875

Doostmohammadi, A., Ardekani, A.M., 2014. Reorientation of elongated particles at density interfaces. Phys. Rev. E 90, 033013. https://doi.org/10.1103/PhysRevE.90.033013

Durante, S., Oliveri, P., Nair, R., Sparnocchia, S., 2021. Mixing in the Tyrrhenian Interior Due to Thermohaline Staircases. Front. Mar. Sci. 8, 672437. https://doi.org/10.3389/fmars.2021.672437

Durante, S., Schroeder, K., Mazzei, L., Pierini, S., Borghini, M., Sparnocchia, S., 2019. Permanent Thermohaline Staircases in the Tyrrhenian Sea. Geophysical Research Letters 46, 1562–1570. https://doi.org/10.1029/2018GL081747

Falco, P., Trani, M., Zambianchi, E., 2016. Water mass structure and deep mixing processes in the Tyrrhenian Sea: Results from the VECTOR project. Deep Sea Research Part I: Oceanographic Research Papers 113, 7–21. https://doi.org/10.1016/j.dsr.2016.04.002

Ferron, B., Bouruet Aubertot, P., Cuypers, Y., Schroeder, K., Borghini, M., 2017. How important are diapycnal mixing and geothermal heating for the deep circulation of the Western Mediterranean? Geophysical Research Letters 44, 7845–7854. https://doi.org/10.1002/2017GL074169

Fuda, J. -L., Etiope, G., Millot, C., Favali, P., Calcara, M., Smriglio, G., Boschi, E., 2002. Warming, salting and origin of the Tyrrhenian Deep Water. Geophysical Research Letters 29. https://doi.org/10.1029/2001GL014072

Ghiglione, J.-F., Conan, P., Pujo-Pay, M., 2009. Diversity of total and active free-living vs. particle-attached bacteria in the euphotic zone of the NW Mediterranean Sea. FEMS Microbiology Letters 299, 9–21. https://doi.org/10.1111/j.1574-6968.2009.01694.x

Giering, S.L.C., Cavan, E.L., Basedow, S.L., Briggs, N., Burd, A.B., Darroch, L.J., Guidi, L., Irisson, J.-O., Iversen, M.H., Kiko, R., Lindsay, D., Marcolin, C.R., McDonnell, A.M.P., Möller, K.O., Passow, U., Thomalla, S., Trull, T.W., Waite, A.M., 2020. Sinking Organic Particles in the Ocean—Flux Estimates From in situ Optical Devices. Front. Mar. Sci. 6, 834. https://doi.org/10.3389/fmars.2019.00834

Guidi, L., Stemmann, L., Jackson, G.A., Ibanez, F., Claustre, H., Legendre, L., Picheral, M., Gorskya, G., 2009. Effects of phytoplankton community on production, size, and export of large aggregates: A world-ocean analysis. Limnology & Oceanography 54, 1951–1963. https://doi.org/10.4319/lo.2009.54.6.1951

Hill, P.S., Boss, E., Newgard, J.P., Law, B.A., Milligan, T.G., 2011. Observations of the sensitivity of beam attenuation to particle size in a coastal bottom boundary layer. J. Geophys. Res. 116, C02023. https://doi.org/10.1029/2010JC006539

Iacono, R., Napolitano, E., Marullo, S., Artale, V., Vetrano, A., 2013. Seasonal Variability of the Tyrrhenian Sea Surface Geostrophic Circulation as Assessed by Altimeter Data. Journal of Physical Oceanography 43, 1710–1732. https://doi.org/10.1175/JPO-D-12-0112.1

Iacono, R., Napolitano, E., Palma, M., Sannino, G., 2021. The Tyrrhenian Sea Circulation: A Review of Recent Work. Sustainability 13, 6371. https://doi.org/10.3390/su13116371

IOC, SCOR and IAPSO, 2010. The international thermodynamic equation of seawater – 2010: Calculation and use of thermodynamic properties.

Johannessen, O.M., Lee, O.S., 1974. A deep stepped thermo-haline structure in the Mediterranean. Deep Sea Research and Oceanographic Abstracts 21, 629–639. https://doi.org/10.1016/0011-7471(74)90047-3

Kapelonis, Z., Siapatis, A., Machias, A., Somarakis, S., Markakis, K., Giannoulaki, M., Badouvas, N., Tsagarakis, K., 2023. Seasonal patterns in the mesopelagic fish community and associated deep scattering layers of an enclosed deep basin. Sci Rep 13, 17890. https://doi.org/10.1038/s41598-023-44765-5

Karl, D.M., Knauer, G.A., Martin, J.H., 1988. Downward flux of particulate organic matter in the ocean: a particle decomposition paradox. Nature 332, 438–441. https://doi.org/10.1038/332438a0

Kermabon, C., Lherminier, P., Le Bot, P., Gaillard, F., 2018. Chaine Automatisée de Suivi des Courantomètres Acoustiques Doppler Embarqués - Cascade V7.2: Logiciel de validation et de visualisation des mesures ADCP de coque.

Kiko, R., Picheral, M., Antoine, D., Babin, M., Berline, L., Biard, T., Boss, E., Brandt, P., Carlotti, F., Christiansen, S., Coppola, L., De La Cruz, L., Diamond-Riquier, E., Durrieu De Madron, X., Elineau, A., Gorsky, G., Guidi, L., Hauss, H., Irisson, J.-O., Karp-Boss, L., Karstensen, J., Kim, D., Lekanoff, R.M., Lombard, F., Lopes, R.M., Marec, C., McDonnell, A.M.P., Niemeyer, D., Noyon, M., O'Daly, S.H., Ohman, M.D., Pretty, J.L., Rogge, A., Searson, S., Shibata, M., Tanaka, Y., Tanhua, T., Taucher, J., Trudnowska, E., Turner, J.S., Waite, A., Stemmann, L., 2022. A global marine particle size distribution dataset obtained with the Underwater Vision Profiler 5. Earth Syst. Sci. Data 14, 4315–4337. https://doi.org/10.5194/essd-14-4315-2022

Kindler, K., Khalili, A., Stocker, R., 2010. Diffusion-limited retention of porous particles at density interfaces. Proc. Natl. Acad. Sci. U.S.A. 107, 22163–22168. https://doi.org/10.1073/pnas.1012319108

Kiørboe, T., 2001. Formation and fate of marine snow: small-scale processes with large- scale implications. Sci. mar. 65, 57–71. https://doi.org/10.3989/scimar.2001.65s257

Kunze, E., 2003. A review of oceanic salt-fingering theory. Progress in Oceanography 56, 399–417. https://doi.org/10.1016/S0079-6611(03)00027-2

Maggi, F., 2013. The settling velocity of mineral, biomineral, and biological particles and aggregates in water: SPM settling velocity in water. J. Geophys. Res. Oceans 118, 2118–2132. https://doi.org/10.1002/jgrc.20086

McCave, I.N., 1984. Size spectra and aggregation of suspended particles in the deep ocean. Deep Sea Research Part A. Oceanographic Research Papers 31, 329–352. https://doi.org/10.1016/0198-0149(84)90088-8

McCave, I.N., 1975. Vertical flux of particles in the ocean. Deep Sea Research and Oceanographic Abstracts 22, 491–502. https://doi.org/10.1016/0011-7471(75)90022-4

Millot, C., Taupier-Letage, I., 2005. Circulation in the Mediterranean Sea, in: Saliot, A. (Ed.), The Mediterranean Sea, Handbook of Environmental Chemistry. Springer Berlin Heidelberg, Berlin, Heidelberg, pp. 29–66. https://doi.org/10.1007/b107143

Molcard, R., Tait, R.I., 1977. The steady state of the step structure in the Tyrrhenian Sea, in: A Voyage of Discovery, George Deacon 70th Anniversary. Oxford, pp. 221–233.

Mrokowska, M.M., 2018. Stratification-induced reorientation of disk settling through ambient density transition. Sci Rep 8, 412. https://doi.org/10.1038/s41598-017-18654-7

Mullison, J., 2017. Backscatter Estimation Using Broadband Acoustic Doppler Current Profilers-Updated.

Nagata, T., Kirchman, D.L., 1997. Roles of Submicron Particles and Colloids in Microbial Food Webs and Biogeochemical Cycles within Marine Environments, in: Advances in Microbial Ecology. Springer, Boston, MA.

Newton, P.P., Liss, P.S., 1990. Particles in the oceans (and other natural waters). Science Progress (1933-) 74, 91–114.

Omand, M.M., Govindarajan, R., He, J., Mahadevan, A., 2020. Sinking flux of particulate organic matter in the oceans: Sensitivity to particle characteristics. Sci Rep 10, 5582. https://doi.org/10.1038/s41598-020-60424-5

Peña, M., 2024. Atlantic versus Mediterranean deep scattering layers around the Iberian peninsula. Progress in Oceanography 221, 103211. https://doi.org/10.1016/j.pocean.2024.103211

Picheral, M., Guidi, L., Stemmann, L., Karl, D.M., Iddaoud, G., Gorsky, G., 2010. The Underwater Vision Profiler 5: An advanced instrument for high spatial resolution studies of particle size spectra and zooplankton. Limnology & Ocean Methods 8, 462–473. https://doi.org/10.4319/lom.2010.8.462

Prairie, J., Ziervogel, K., Arnosti, C., Camassa, R., Falcon, C., Khatri, S., McLaughlin, R., White, B., Yu, S., 2013. Delayed settling of marine snow at sharp density transitions driven by fluid entrainment and diffusion-limited retention. Mar. Ecol. Prog. Ser. 487, 185–200. https://doi.org/10.3354/meps10387

Pujo-Pay, M., Durrieu de Madron, X., Conan, P., 2020. PERLE3 cruise, R/V Pourquoi Pas ?. https://doi.org/10.17600/18001342

Radko, T., 2013. Double-diffusive convection. Cambridge university press, Cambridge.

Radko, T., Bulters, A., Flanagan, J.D., Campin, J.-M., 2014. Double-Diffusive Recipes. Part I: Large-Scale Dynamics of Thermohaline Staircases. Journal of Physical Oceanography 44, 1269–1284. https://doi.org/10.1175/JPO-D-13-0155.1

Radko, T., Smith, D.P., 2012. Equilibrium transport in double-diffusive convection. J. Fluid Mech. 692, 5–27. https://doi.org/10.1017/jfm.2011.343

Rinaldi, E., Buongiorno Nardelli, B., Zambianchi, E., Santoleri, R., Poulain, P. -M., 2010. Lagrangian and Eulerian observations of the surface circulation in the Tyrrhenian Sea. J. Geophys. Res. 115, 2009JC005535. https://doi.org/10.1029/2009JC005535

Schroeder, K., Ben Ismail, S., Bensi, M., Bosse, A., Chiggiato, J., Civitarese, G., Falcieri M, F., Fusco, G., Gačić, M., Gertman, I., Kubin, E., Malanotte-Rizzoli, P., Martellucci, R., Menna, M., Ozer, T., Taupier-Letage, I., Vargas-Yáñez, M., Velaoras, D., Vilibić, I., 2024. A consensus-based, revised and comprehensive catalogue for Mediterranean water masses acronyms. Mediterr. Mar. Sci. 25, 783–791. https://doi.org/10.12681/mms.38736

Sparnocchia, S., Gasparini, G.P., Astraldi, M., Borghini, M., Pistek, P., 1999. Dynamics and mixing of the Eastern Mediterranean outflow in the Tyrrhenian basin. Journal of Marine Systems 20, 301–317. https://doi.org/10.1016/S0924-7963(98)00088-8

Taillandier, V., Prieur, L., D'Ortenzio, F., Ribera d'Alcalà, M., Pulido-Villena, E., 2020. Profiling float observation of thermohaline staircases in the western Mediterranean Sea and impact on nutrient fluxes. Biogeosciences 17, 3343–3366. https://doi.org/10.5194/bg-17-3343-2020

Thiele, S., Fuchs, B.M., Amann, R., Iversen, M.H., 2015. Colonization in the Photic Zone and Subsequent Changes during Sinking Determine Bacterial Community Composition in Marine Snow. Appl Environ Microbiol 81, 1463–1471. https://doi.org/10.1128/AEM.02570-14

Thurnherr, A.M., 2022. How to Process LADCP Data For Vertical Velocity (w) and Derive Parameterized Estimates for Turbulent Kinetic Energy Dissipation (ε) using LADCP w Software V2.2.

Thurnherr, A.M., 2021. How To Process LADCP Data With the LDEO Software (Version IX.14).

Van Der Boog, C.G., Koetsier, J.O., Dijkstra, H.A., Pietrzak, J.D., Katsman, C.A., 2021. Global dataset of thermohaline staircases obtained from Argo floats and Ice-Tethered Profilers. Earth Syst. Sci. Data 13, 43–61. https://doi.org/10.5194/essd-13-43-2021

Verso, L., Reeuwijk, M.V., Liberzon, A., 2019. Transient stratification force on particles crossing a density interface. International Journal of Multiphase Flow 121, 103109. https://doi.org/10.1016/j.ijmultiphaseflow.2019.103109

WET Labs, Inc., 2011. Transmissometer C-Star User's Guide.

Yang, S., Zhang, K., Song, H., Ruddick, B., Liu, M., Meng, L., 2024. Disruptions in thermohaline staircases caused by subsurface mesoscale eddies in the eastern Caribbean Sea. Commun Earth Environ 5, 408. https://doi.org/10.1038/s43247-024-01577-3

Zodiatis, G., Gasparini, G.P., 1996. Thermohaline staircase formations in the Tyrrhenian Sea. Deep Sea Research Part I: Oceanographic Research Papers 43, 655–678. https://doi.org/10.1016/0967-0637(96)00032-5

Data Availability Statement

The CTD and ADCP data used in this study are available at https://doi.org/10.17600/18001342. The UVP data are available at https://ecopart.obs-vlfr.fr.

Author Contributions

Conceptualization and Methodology, XDDM, PB and MPP; Writing – Original Draft Preparation, XDDM and PB; Writing – Review & Editing, All.

Acknowledgements

This study benefited from the data obtained during the PERLE-3 cruise with the R/V Pourquoi-Pas? and was supported by the MISTRALS-MERMEX project. We thank Valérie Domien for producing the graphical abstract.

Competing interests

The authors declare that they have no conflict of interest.

Appendix A

Table A1 Mean abundance (#/L) percentage, and cumulative percentage by size class of UVP between 80 and 2000 mm for all stations between the surface and 2000 m depth

Size class	Abundance (# L^{-1})	Percentage	Cumulative percentage
80.6-102 µm	26.272	45.617	45.62
102-128 µm	10.465	18.171	63.79
128-161 µm	5.547	9.631	73.42
161-203 µm	8.542	14.832	88.25
203-256 µm	3.13	5.435	93.68
256-323 µm	1.944	3.375	97.06
323-406 µm	0.985	1.710	98.77
406-512 µm	0.391	0.679	99.45
512-645 µm	0.169	0.293	99.74
645-813 µm	0.078	0.135	99.88
0.813-1020 µm	0.038	0.066	99.94
1.02-1290 µm	0.018	0.031	99.98
1.29-1630 µm	0.009	0.016	99.99
1630-2050 µm	0.005	0.009	100.00

Page 22 : [1] a supprimé	**Xavier Durrieu de Madron**	**08/03/2025 13:33:00**

Page 23 : [2] a mis en forme	**Xavier Durrieu de Madron**	**08/03/2025 13:34:00**

Police :(Par défaut) Times New Roman, 12 pt

Page 23 : [3] a mis en forme	**Xavier Durrieu de Madron**	**08/03/2025 13:34:00**

Police :(Par défaut) Times New Roman, 12 pt

Page 23 : [4] a mis en forme	**Xavier Durrieu de Madron**	**08/03/2025 14:28:00**

Anglais (E.U.)

Page 23 : [5] a mis en forme	**Xavier Durrieu de Madron**	**08/03/2025 14:28:00**

Anglais (E.U.)

Page 23 : [6] a mis en forme	**Xavier Durrieu de Madron**	**08/03/2025 13:33:00**

Non Surlignage

Page 23 : [7] a mis en forme	**Xavier Durrieu de Madron**	**08/03/2025 13:33:00**

Non Surlignage

Page 23 : [8] a mis en forme	**Xavier Durrieu de Madron**	**08/03/2025 13:33:00**

Exposant

Page 23 : [9] a mis en forme	**Xavier Durrieu de Madron**	**08/03/2025 13:33:00**

Non Surlignage

Page 23 : [10] a mis en forme	**Xavier Durrieu de Madron**	**08/03/2025 13:33:00**

Exposant

Page 23 : [11] a mis en forme	**Xavier Durrieu de Madron**	**08/03/2025 13:33:00**

Non Surlignage

Page 23 : [12] a mis en forme	**Xavier Durrieu de Madron**	**08/03/2025 13:33:00**

Non Surlignage

Page 23 : [13] a mis en forme	**Xavier Durrieu de Madron**	**08/03/2025 13:33:00**

Non Surlignage

Page 23 : [14] a mis en forme	**Xavier Durrieu de Madron**	**08/03/2025 13:33:00**

Indice

Page 23 : [15] a mis en forme	**Xavier Durrieu de Madron**	**08/03/2025 13:33:00**

Non Surlignage

Page 23 : [16] a mis en forme	**Xavier Durrieu de Madron**	**08/03/2025 13:33:00**

Exposant

Page 23 : [17] a mis en forme	**Xavier Durrieu de Madron**	**08/03/2025 13:33:00**

Indice, Non Surlignage

Page 23 : [18] a mis en forme	**Xavier Durrieu de Madron**	**08/03/2025 13:33:00**

Non Surlignage

Page 23 : [19] a mis en forme	**Xavier Durrieu de Madron**	**08/03/2025 13:33:00**

Non Surlignage

Page 23 : [20] a mis en forme	**Xavier Durrieu de Madron**	**08/03/2025 13:33:00**

Non Surlignage

Page 23 : [21] a mis en forme	**Xavier Durrieu de Madron**	**08/03/2025 13:33:00**

Non Surlignage

Page 23 : [22] a mis en forme	Xavier Durrieu de Madron	08/03/2025 13:33:00

Non Surlignage

Page 23 : [23] a mis en forme	Xavier Durrieu de Madron	08/03/2025 13:33:00

Indice

Page 23 : [24] a mis en forme	Xavier Durrieu de Madron	08/03/2025 13:33:00

Non Surlignage

Page 23 : [25] a mis en forme	Xavier Durrieu de Madron	08/03/2025 13:33:00

Non Surlignage

Page 23 : [26] a mis en forme	Xavier Durrieu de Madron	10/03/2025 09:15:00

Retrait : Première ligne : 0 cm

Page 23 : [27] a mis en forme	Xavier Durrieu de Madron	08/03/2025 13:33:00

Non Surlignage

Page 23 : [28] a mis en forme	Xavier Durrieu de Madron	08/03/2025 13:33:00

Non Surlignage

Page 23 : [29] a mis en forme	Xavier Durrieu de Madron	08/03/2025 13:33:00

Non Surlignage

Page 23 : [30] a mis en forme	Xavier Durrieu de Madron	08/03/2025 13:33:00

Non Surlignage

Page 23 : [31] a mis en forme	Xavier Durrieu de Madron	08/03/2025 13:33:00

Non Surlignage

Page 23 : [32] a mis en forme	Xavier Durrieu de Madron	08/03/2025 13:33:00

Non Surlignage

Page 23 : [33] a supprimé	Xavier Durrieu de Madron	08/03/2025 14:53:00